Supporting Information for

Environmentally Friendly Nitrogen-Doped Carbon Quantum Dots for Next Generation Solar Cells

Darragh Carolan, Conor Rocks, Dilli Babu Padmanaban, Paul Maguire, Vladimir Svrcek, and Davide Mariotti*

Experimental

Materials/Chemicals:

Citric acid (CA, ≥ 99.5 %) and ethylenediamine (EDA ≥ 99 %), were purchased from Sigma Aldrich Ltd. and stored in ambient atmosphere. All materials and solvents were used as received.

Synthesis and purification of N-CQDs:

The N-CQDs were synthesized by taking advantage of microplasma-liquid interactions. The atmospheric pressure microplasma setup (see Fig. 1) consists of a direct-current (DC) source (Matsusada DC high voltage power supply), a carbon rod as the cathode (length: 100 mm; diameter: 5 mm) which was connected to the current source *via* a 100 kΩ ballast resistor and a hollow nickel tube as the anode (Goodfellow, 99.5 %, outer diameter: 1 mm, wall thickness: 0.1 mm, inner diameter: 0.8 mm).

Typically, citric acid (1.051 g, 7.8 mmol of COOH groups) and ethylenediamine (556 μL, 15.6 mmol NH_2 groups) were dissolved in 10 mL de-ionized (DI) water (1:2 molar ratio of COOH:NH_2). This solution was then transferred to a clean, 20 mL crystallizing dish, the carbon electrode was immersed in the solution while the nickel tube was brought to within 2 mm of the surface of the liquid. The distance between the two electrodes was approximately 2 cm. The microplasma jet was then ignited between the end of the nickel tubing and the surface of the water using a flow of pure helium gas (MKS PR4000B mass flow controller, 60 sccm) and a current of 6 mA between the electrodes. The distance between the nickel tubing and the surface

of the water was adjusted to maintain a constant discharge voltage of 1.3 kV. The reaction was paused and the solution stirred every 10 minutes. The reactions were carried out for 30 minutes in total to give a yield of 1 mg/mL of N-CQDs in water.

Fabrication of solar cells:

Substrates from VisionTek Systems Ltd. were 38 mm in length, 13 mm in width and had a thickness of 0.7 mm. They were fabricated using OLED-quality polished glass and included a patterned strip of indium-doped tin oxide (15 Ω/sq, 150 nm thick, and 2 mm wide) running lengthwise down the middle of the substrate. Before fabrication of devices, substrates were cleaned by successive sonication in propan-2-ol (IPA), immersion in boiling acetone, sonication in fresh IPA, and sonication in DI water for 10 minutes each and finally dried with a nitrogen gun.

A compact TiO_2 hole blocking layer was formed using a sol-gel method. Briefly, titanium isopropoxide (1.56 mL) was added to a clean beaker containing triethanolamine (0.394 g) and ethanol (18 mL). The mixture was stirred on a hotplate at 40 °C for 2 hours. The solution was then left to rest at room temperature overnight. About 100 μL of this solution was then spun-cast onto the pre-patterned ITO coated substrates at 4000 revolutions per minute (RPM) for 30 s. The substrate was heated on a hotplate at 100 °C for 30 min and then in an oven at 350 °C overnight to promote crystallization of the film. This process formed a 40 nm compact layer of anatase TiO_2.

Subsequently, N-CQDs were deposited by spray coating using an atomizer (Sonozap Ultra Sonic Atomizer) operating at a power of 5 W. 5 mL of an N-CQD solution was loaded into a syringe, connected to a pump and flowed through the atomizer at a rate of 0.15 mL/min. The atomizer tip was 8 cm away from the substrate. The substrate was continuously heated on a hotplate at 170 °C throughout deposition and left to dry for 10 minutes after deposition. Gold contacts were deposited orthogonal to the indium-doped tin oxide (ITO) strip, using plasma assisted magnetron sputtering. The plasma was produced at 317 V and 0.15 A. Deposition was

carried out for 50 minutes to give a gold film with a thickness of *ca*. 340 nm. The active area of each cell was 4 mm^2.

Characterization:

Transmission electron microscopy images and selective area electron diffraction patterns were acquired using a high resolution JEOL JEM-2100F field emission electron microscope, and Gatan DualVision 600 Charge-Coupled Device (CCD), operating at an accelerating voltage of 200 keV. TEM samples were prepared by depositing a 40 μL aliquot of the QD dispersion onto a holey carbon-coated copper grid (300 mesh, #S147-3, Agar Scientific), which was allowed to evaporate under ambient conditions. Data for size distribution histograms was acquired by analysis of TEM images of exactly 200 QDs located at different regions of the grid. QD diameter was determined by manual inspection of the digital images.

X-ray diffraction measurements were performed on a Bruker AXS D8Discover instrument using monochromatic Cu Kα X-ray radiation at an accelerating voltage of 40 kV and current of 40 mA. Scans were performed in 0.02 increments and at a scan speed of 20 s per step to give a total acquisition time of 20 hours. Samples were prepared by spray coating colloids with the atomizer on glass substrates.

X-ray photoelectron spectroscopy measurements were carried out using a Kratos Axis Ultra DLD photoelectron spectrometer at ≈ 10^{-9} mbar base pressure. The narrow scan spectra were obtained under high vacuum conditions using a monochromatic Al Kα X-ray radiation at 15 kV and 10 mA with an analyzer pass energy of 20 eV. The N-CQD dispersion was deposited using the atomizer on either plane glass or ITO coated glass substrates. All spectra were acquired at room temperature and binding energies were referenced to the C 1s line at 285 eV. All spectra were corrected using a linear background fitting.

Ultraviolet photoelectron spectroscopy was carried out with a Kratos Axis Ultra DLD spectrometer and measurements were performed at < 2 × 10^{-8} mbar base pressure with He 1 α

(h = 21.22 eV) as the excitation source, a dwell time of 0.1 s with 40 sweeps performed. Samples were prepared by spray coating the N-CQDs on ITO coated glass.

Fourier transform infrared spectra were recorded on a Thermo Scientific Nicolet iS5 spectrometer equipped with an iD5 attenuated total reflection (ATR) accessory. Spectra were recorded on colloids that were spray coated using the atomizer onto glass substrates. Spectra were recorded with a resolution of 2 cm^{-1} and 32 scans were averaged.

Kelvin probe measurements (SKP Kelvin Probe Version Delta 5+, Version 5.05 from KP Technology Ltd., U.K.) were performed to determine the Fermi level of the N-CQDs. This technique measures the contact potential difference (CPD) between the sample surface and a vibrating tip. The work function (ϕ) of the N-CQD film can be measured in comparison to a reference material, in this case gold. A thick film was deposited from colloids that were spray-coated onto ITO-coated glass substrates and the ITO layer was connected to the ground during measurements. All measurements were performed at ambient conditions, the probe was scanned across a 100 µm x 100 µm area, taking measurements at 25 different points in the scanned area, and relative changes in the CPD were recorded. The work function (ϕ) is then calculated using the equation; $\phi_{sample} = \phi_{Au} - CPD_{Au} + CPD_{sample}$where ϕ_{Au} is the work function of Au (5100 meV relative to the vacuum level), CPD_{Au} is the CPD between the tip and the Au surface while CPD_{sample} is the CPD between the tip and the sample surface. An average value and corresponding standard deviation were calculated from the 25 measurements for each sample.

Ambient photoemission spectroscopy (APS) was carried out with a similar instrument with a module containing a high intensity deuterium source coupled with a motorized grating monochromator. The sample is illuminated with a 4-5 mm diameter light spot derived from the tuneable monochromated D2 lamp. Nitrogen gas is used to suppress the production of ozone in the DUV spectrometer and the energy range of incident photons is typically 3-7 eV. The raw photoemission data are corrected for detector offset; intensity normalized, then processed by either a square or cube root power law.

UV-Vis absorption spectra were recorded using a PerkinElmer Lambda 650 S spectrophotometer equipped with a 150 mm integrating sphere. Photoluminescence spectra were recorded using an Agilent Cary Eclipse spectrophotometer. Spectra for both UV-Vis and PL were recorded at room temperature using quartz cuvettes (1 cm) and corrected for the solvent absorption or emission. Data for the Tauc plots were acquired as follows. The transmission (T) of the colloidal samples was obtained in the normal way in the sampling compartment in front of the integrating sphere. This does not account for scattering or reflectance of the sample. The transmission of the samples was also attained inside the integrating sphere (T_{IS}). This considers sample reflectance and scattering ($T + R + S$). The absorption coefficient (α) was then determined using the following formula:

$$\alpha = \frac{1 - T_{IS}}{L(1 - T)}(-lnT)$$

Where T_{IS} is the transmission taken inside the integrating sphere ($T_{IS} = T + R + S$), L is the path length (spectra were recorded on colloids in a 1 cm cuvette), and T is the transmission taken in the normal fashion in the front compartment which neglects reflection and scattering. $\alpha h\nu^{1/2}$ was plotted as a function of energy, and the bandgap determined from the intersection with the x-axis of a linear fit to the data.

For absolute quantum yield measurements, an integration sphere attached to a Horiba Jobin Yvon fluoromax-4 spectrometer was used to collect the PL of the N-CQD film. For excitation, a Xe lamp with a double monochromator was used, and the PL was detected by a charge-coupled detector (CCD) mounted on a spectrograph *via* coupled ultraviolet-grade optical fiber. The excitation wavelength was selected through the monochromator. The emission spectra from the sample (N-CQDs on quartz) and the reference (quartz only) were measured, and the number of emitted photons was then calculated from spectral integration. The number of absorbed photons was calculated using reduction of the excitation spectrum and comparing the sample and reference. The absolute QY is obtained as the ratio of the number of emitted photons

to the number of absorbed photons. Measurements were carried out with an excitation wavelength of 420 nm (3 eV), performed in triplicates, and the average value was reported.

Electrical characterization of the solar cell devices was performed using a Keithley 2400 SourceMeter and running Tracer 2 software. Cells were 0.04 cm^2 in size and illuminated at 1 sun, AM 1.5 (1000 W/cm^2) with a LOT QuantumDesign solar simulator light source. The J-V characteristics of the solar cells were evaluated at room temperature in air. In all cases, the irradiance was calibrated using a standard 4 cm^2 Si solar cell.

Results and discussion

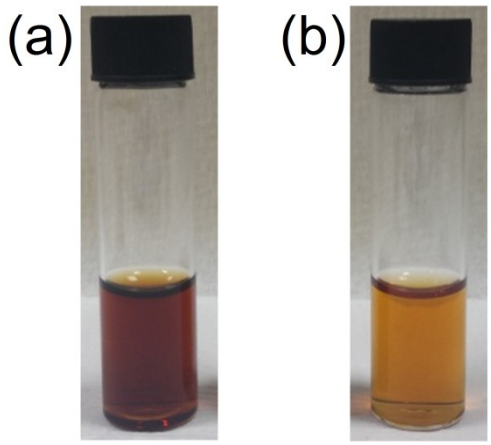

Fig. ESI1. Digital images of N-CQDs produced with the plasma as (a) anode and (b) cathode. 3.2x2.3 in; single column, 600 dpi

Formation Mechanism:

To investigate the formation mechanism, various different experiments were performed. With the plasma as the cathode, fewer QDs were formed which implies that the reaction was sensitive to the properties of the plasma, see Fig. ESI1. The microplasma anode transfers positive charges to the solution while the plasma cathode transfers electrons. Furthermore, different species like ultraviolet radiation, radicals, electrons, and ions contribute to extremely complex conditions. Because conditions at the anode are more complicated and different non-electrochemical reactions can occur, the microplasma anode provides unique circumstances for preparing N-CQDs, that are different to other reported plasma methods. When the reaction was carried out with a platinum electrode replacing the plasma anode, the color of the solution did not change

meaning that no N-CQDs formed, it was not a simple electrochemical reaction, and that the presence of the microplasma was necessary. The suggested formation mechanism is the plasma enhanced condensation reaction between OH containing carbon precursor and nitrogen precursor containing NH_2 groups.[1,2] The carbon molecules can self-assemble and condensation reactions occur to form an extended carbon framework. The N atoms enter the QD framework by forming a pyrrolic structure (see FTIR and XPS discussion in the manuscript) through further intramolecular dehydroxylation between adjacent carboxyl and amide groups. In particular, the decrease of the C=O peak in the FTIR upon increasing the amount of nitrogen, suggests the consumption of –COOH groups due to the dehydrolysis reaction discussed above, while the increase of the C=N peak implies the successful N doping with formation of pyrrolic ring-like structures. The changing oxygen and nitrogen XPS atomic percentages, as well as the presence of pyrrolic N further support this formation mechanism. The microplasma as the anode significantly accelerates the rate of this reaction, allowing for the low temperature, rapid synthesis of highly luminescent N-CQDs.

Solutions with a fixed amount of water and CA, but varying amounts of EDA were treated with the microplasma. When no EDA was present, only a very minor color change was observed from colorless to a very pale straw yellow color, Fig. ESI2 (a). When 139 µL EDA (1:0.5 molar ratio of COOH:NH_2) was added to the initial solution and then treated with the microplasma, the color changed to a darker yellow (see Fig. ESI2 (b)). This indicated that the addition of EDA drastically improved the final amount of N-CQDs produced. As the amount of EDA added was further increased, different colored final solutions were obtained. 278 µL EDA (1:1 ratio COOH:NH_2) produced an orange color, 556 µL EDA (1:2 ratio COOH:NH_2) produced a dark brown color while 834 µL EDA (1:3 ratio COOH:NH_2) gave a less intense brownish-red color, see Fig. ESI2 (c-e). A 1:2 ratio of COOH:NH_2 (556 µL EDA) gave the darkest color suggesting that these reaction conditions produced the greatest amount of N-CQDs, whereas increasing the ratio further to 1:3 COOH:NH_2 gave a less intense color indicating that too much EDA in the

initial solution actually inhibits the reaction. Moreover, processing a solution with only EDA present (Fig. ESI2 (f)) gave no observable color change, implying that citric acid is necessary for the formation of the N-CQDs.

The reaction could also be carried out in different solvent mixtures. Water was mixed with the same amount of ethanol, propan-2-ol or acetone. The precursors were then added and the mixtures treated with the microplasma. As seen in Fig. ESI3 (a-d) the H_2O-EtOH mixture produced an orange color, H_2O-IPA mixtures gave a dark orange while H_2O-acetone generated a light brown solution. These results demonstrate that the microplasma assisted synthesis of N-CQDs was simple, rapid, and inexpensive and could be carried out with a range initial solvent mixtures.

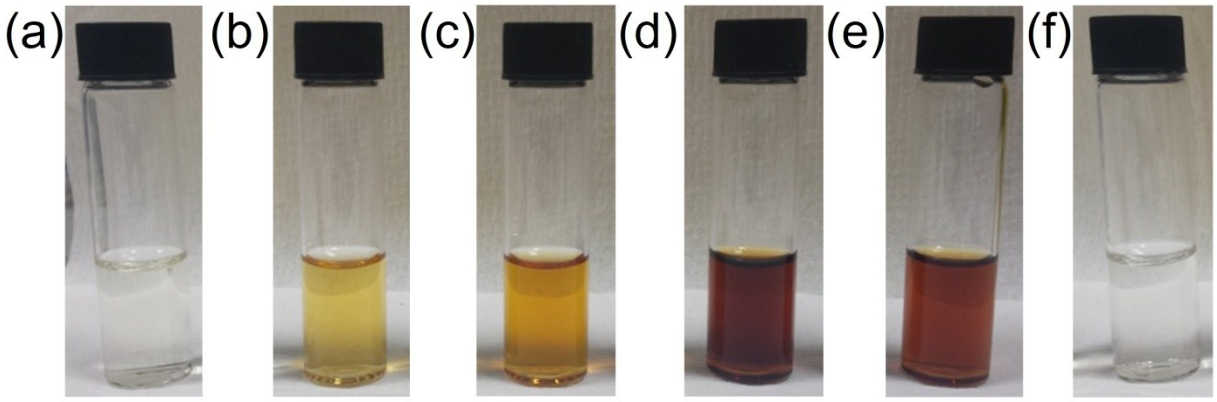

Fig. ESI2. Digital images of N-CQDs produced with different amounts of ethylenediamine in the initial solution; (a) None, (b) 139 µL, (c) 278 µL, (d) 556 µL, (e) 834 µL and (f) EDA alone with no citric acid.. 7x2.3 in; double column, 600 dpi

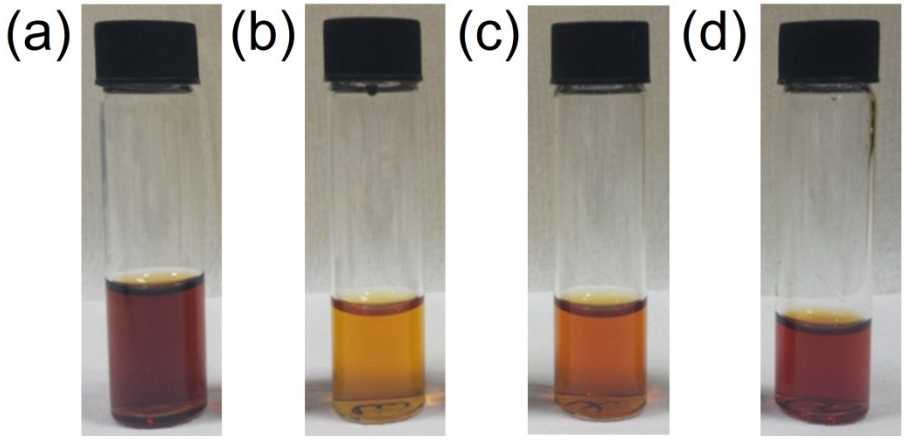

Fig. ESI3. Digital images of N-CQDs produced with different solvent mixtures; (a) water, (b) water:ethanol, (c) water:propan-2-ol and (d) water:acetone. 5x2.3 in; double column, 600 dpi

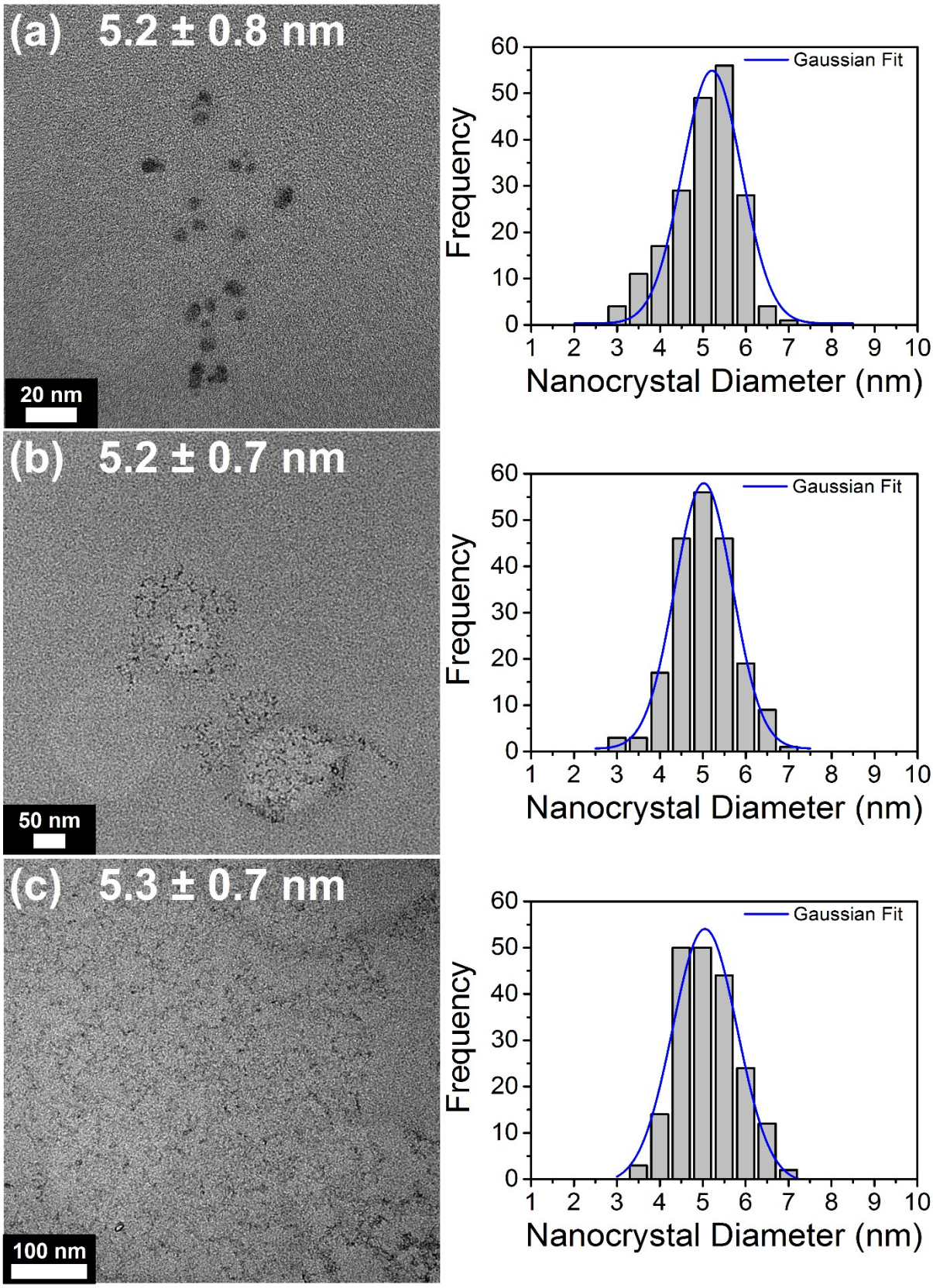

Fig. ESI4. TEM images of the N-CQDs synthesized with (a) 139 µL, (b) 278 µL and (c) 834 µL EDA and corresponding histograms on the right. 6.4x8.8 in; double column, 600 dpi

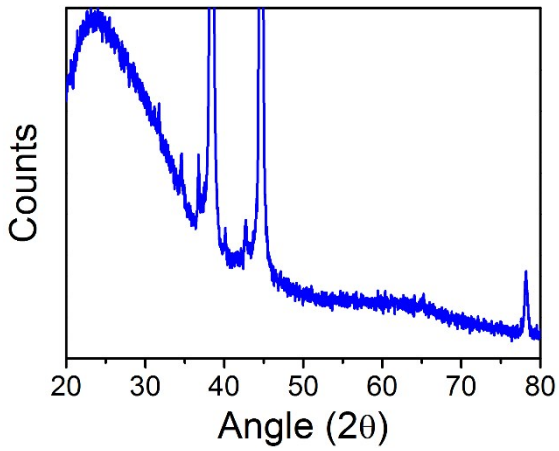

Fig. ESI5. XRD pattern from the N-CQDs on glass. 3.2x2.3 in; single column, 600 dpi

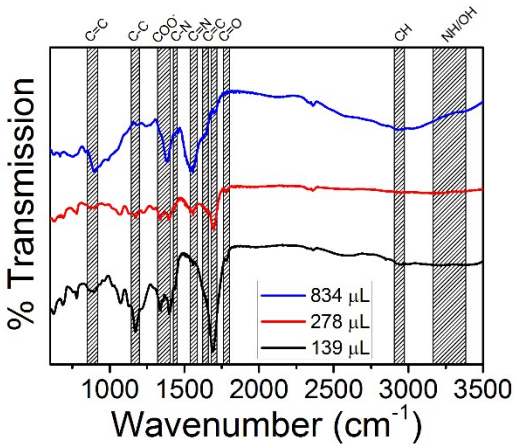

Fig. ESI6. FTIR spectra for the other N-CQDs samples. 2.9x2.3 in; single column, 600 dpi

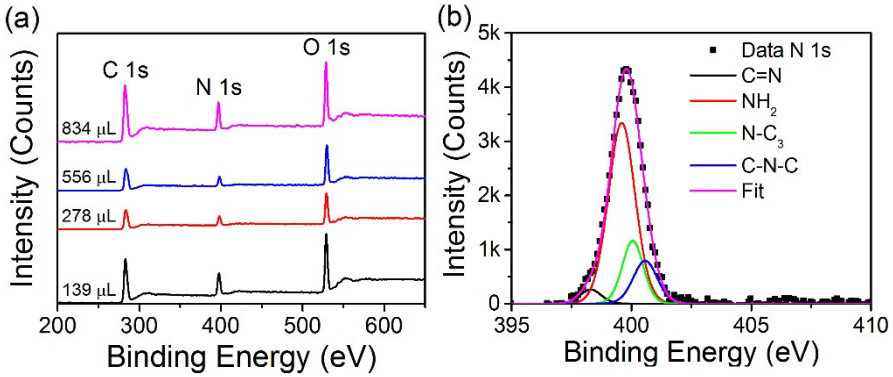

Fig. ESI7. (a) XPS survey spectra for all the samples, (b) high resolution spectrum of the N 1s region for N-CQDs synthesized with 834 µL EDA. 4.6x2 in; double column, 600 dpi

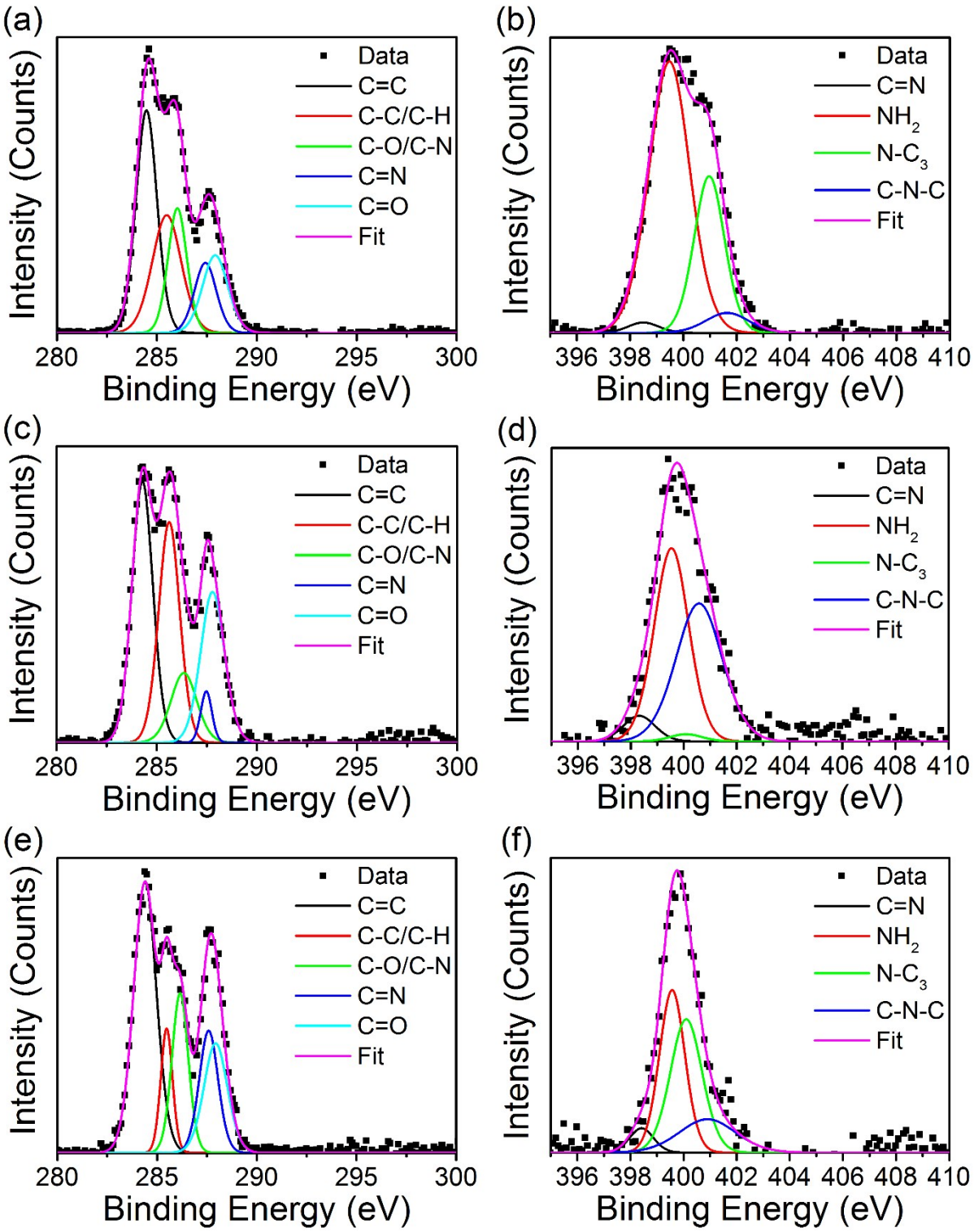

Fig. ESI8. High resolution XPS C 1s and N 1s spectra for the other samples synthesized with (a), (b) 556 µL EDA, (c), (d) 278 µL EDA and (e), (f) 139 µL EDA. 6.4x8 in; double column, 600 dpi

From the data shown in Fig. 4 we can calculate the bandgap *via* a complimentary method. In the Tauc plot, $\alpha h\nu^{1/r}$ is plotted against energy ($h\nu$), where the factor r represents the nature of the optical transition. The absorption coefficient (α) can then be expressed as:

$$\alpha = (\frac{A}{h\nu})(h\nu - E_g) \qquad [1]$$

Where A is a constant, $h\nu$ is the energy of photons, and E_g is band gap. From [1], we then have:

$$\frac{d(ln(\alpha h\nu))}{d(h\nu)} = \frac{r}{h\nu - E_g} \qquad [2]$$

Therefore, if we plot $\frac{d(ln(\alpha h\nu))}{d(h\nu)}$ vs. $h\nu$, a discontinuity can be observed where $h\nu - E_g = 0$, *i.e.* at the bandgap value. Using the data shown in Fig. 4, the differential of $\alpha h\nu$ is taken with respect to $h\nu$ and is plotted against $h\nu$, see Fig. ESI9 (a).

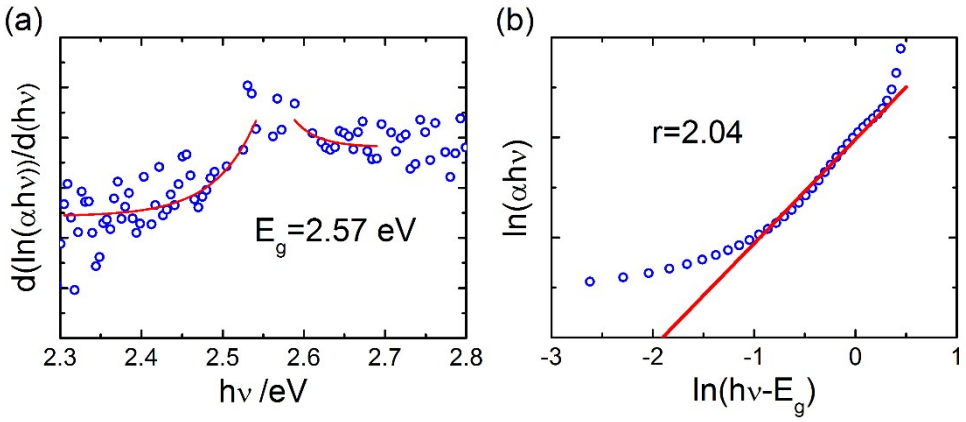

Fig. ESI9. Plot of $d(ln(\alpha h\nu))/d(h\nu)$ vs $h\nu$ for the N-CQDs and (b) plot of $ln(\alpha h\nu)$ vs $ln(h\nu - E_g)$ for $E_g = 2.57$. 5x2.16 in; single column, 600 dpi

As can be seen, the discontinuity occurs at 2.57 eV, in close agreement with the bandgap determined from the Tauc plot (Fig. 4(b)). Furthermore, we can confirm the transition nature by determining the value of r with the following relation:

$$ln(\alpha h\nu) = ln(A) + r ln(h\nu - E_g) \qquad [3]$$

Plotting $ln(\alpha h\nu)$ against $ln(h\nu - E_g)$ and taking the gradient of the line, as seen in Fig. ESI9 (b), gives a value of $r = 2.04$ which is sufficiently close to 2; the expected value for an indirect transition.

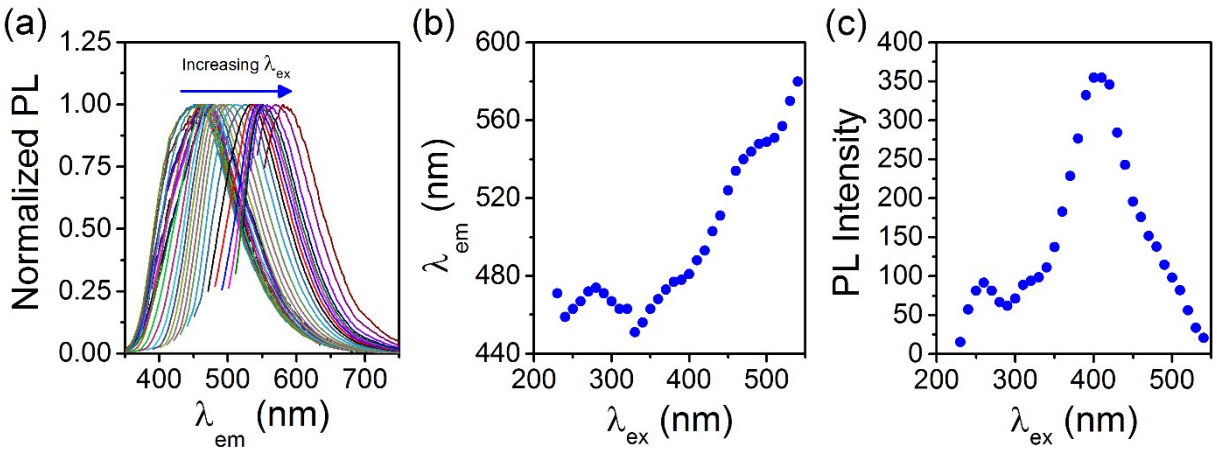

Fig. ESI10. Photoluminescence characterization of N-CQDs with 12.7 % (556 µL EDA) nitrogen. (a) normalized PL spectra, (b) variation in the emission wavelength position as a function of excitation wavelength, (c) change in the PL intensity as a function of excitation wavelength. 6.4x2.4 in; double column, 600dpi

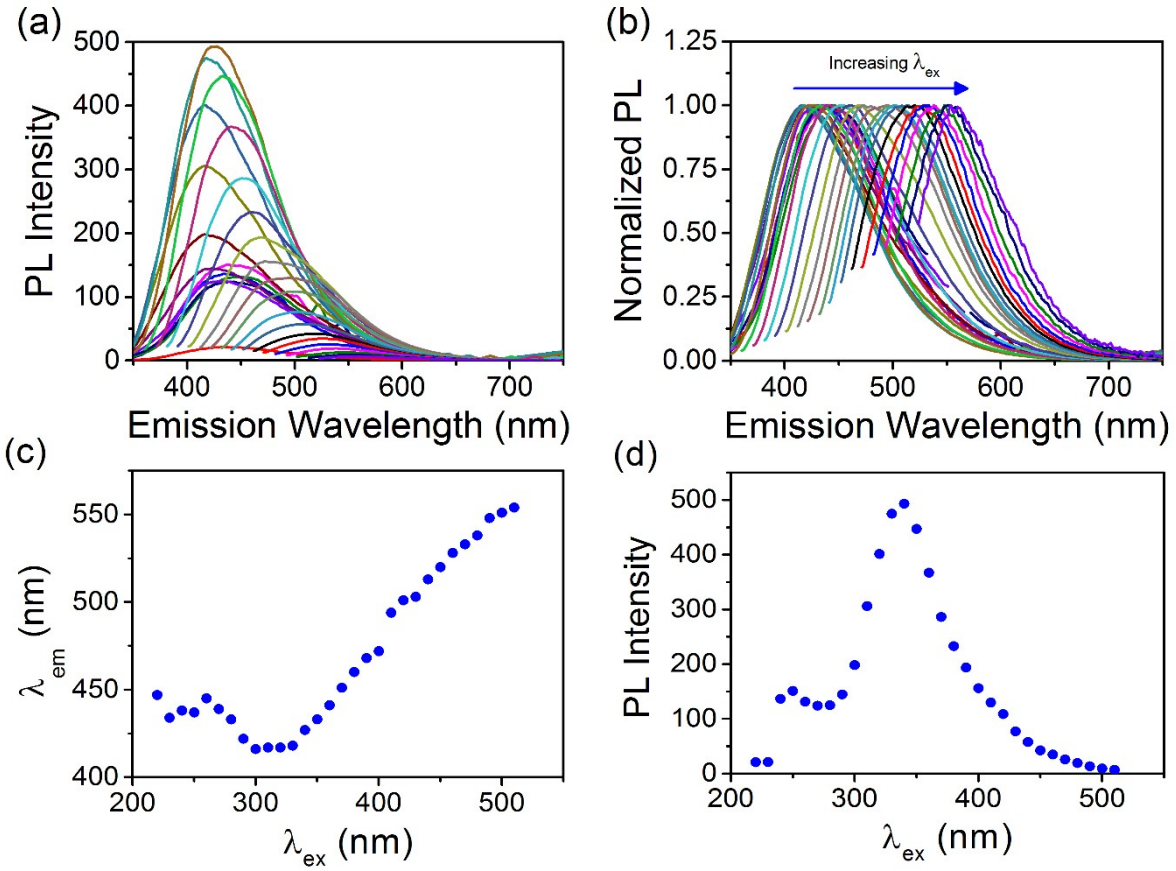

Fig. ESI11. Photoluminescence characterization of N-CQDs with 9.4 % (139 µL EDA) nitrogen. (a) PL spectra at different excitation wavelengths, (b) normalized spectra, (c) variation in the emission wavelength position as a function of excitation wavelength, (d) change in the PL intensity as a function of excitation wavelength. 6.4x4.6 in; double column, 600dpi

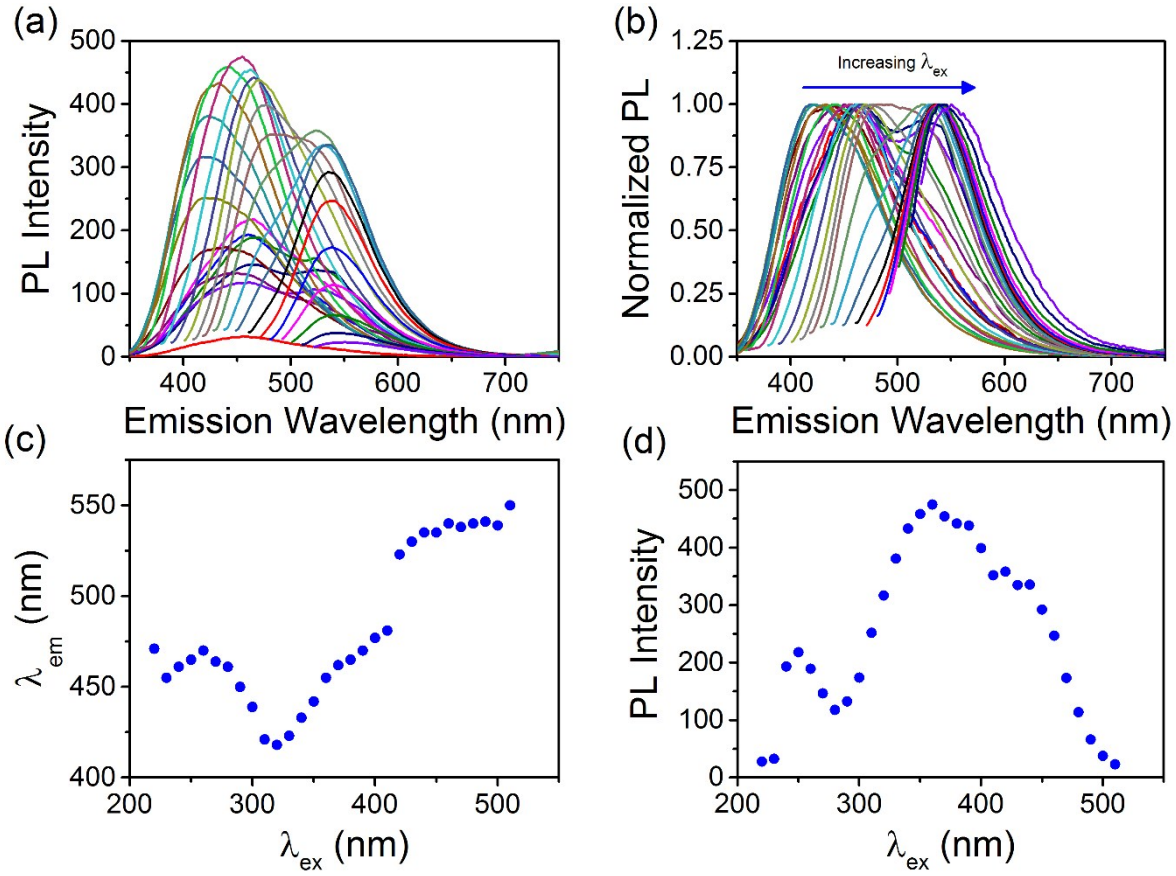

Fig. ESI12. Photoluminescence characterization of N-CQDs with 11.9 % (278 µL EDA) nitrogen. (a) PL spectra at different excitation wavelengths, (b) normalized spectra, (c) variation in the emission wavelength position as a function of excitation wavelength, (d) change in the PL intensity as a function of excitation wavelength. 6.4x4.6 in; double column, 600dpi

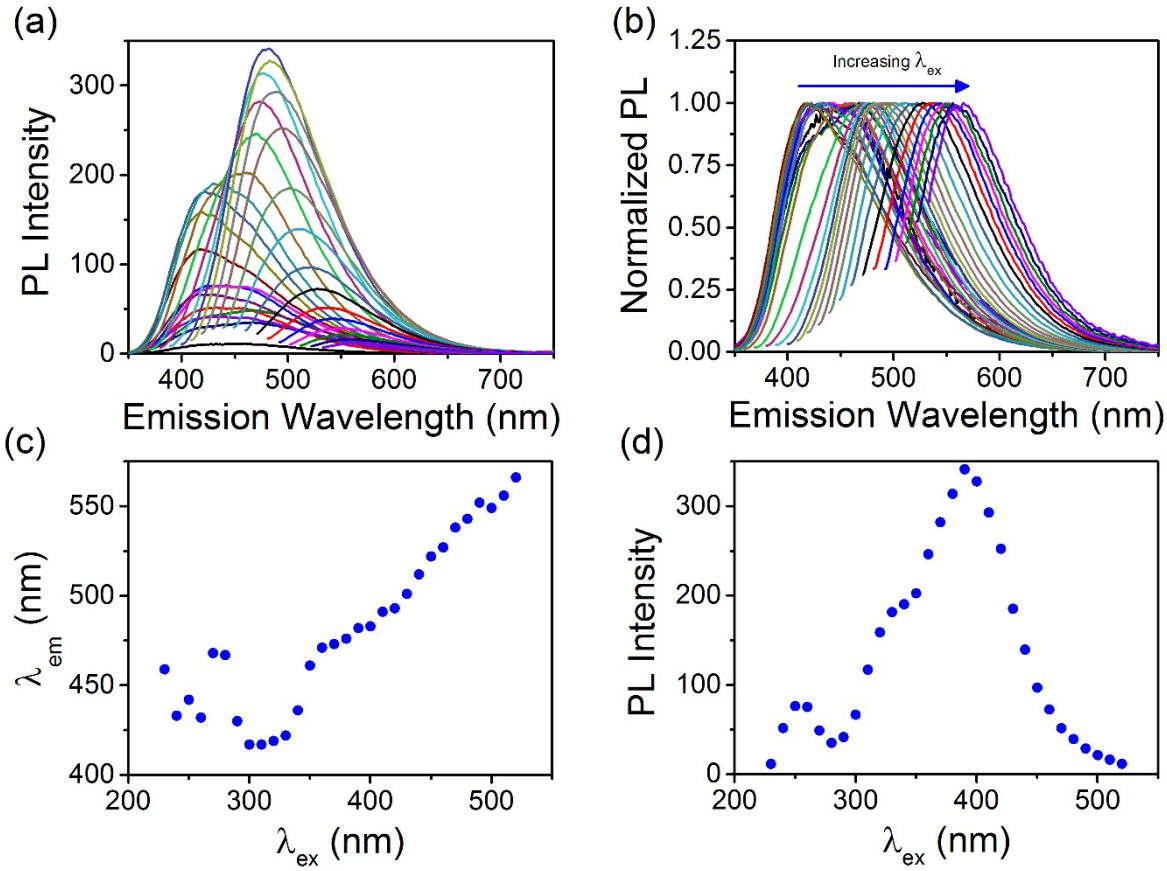

Fig. ESI13. Photoluminescence characterization of N-CQDs with 15.5 % (834 µL EDA) nitrogen. (a) PL spectra at different excitation wavelengths, (b) normalized spectra, (c) variation in the emission wavelength position as a function of excitation wavelength, (d) change in the PL intensity as a function of excitation wavelength. 6.4x4.6 in; double column, 600dpi

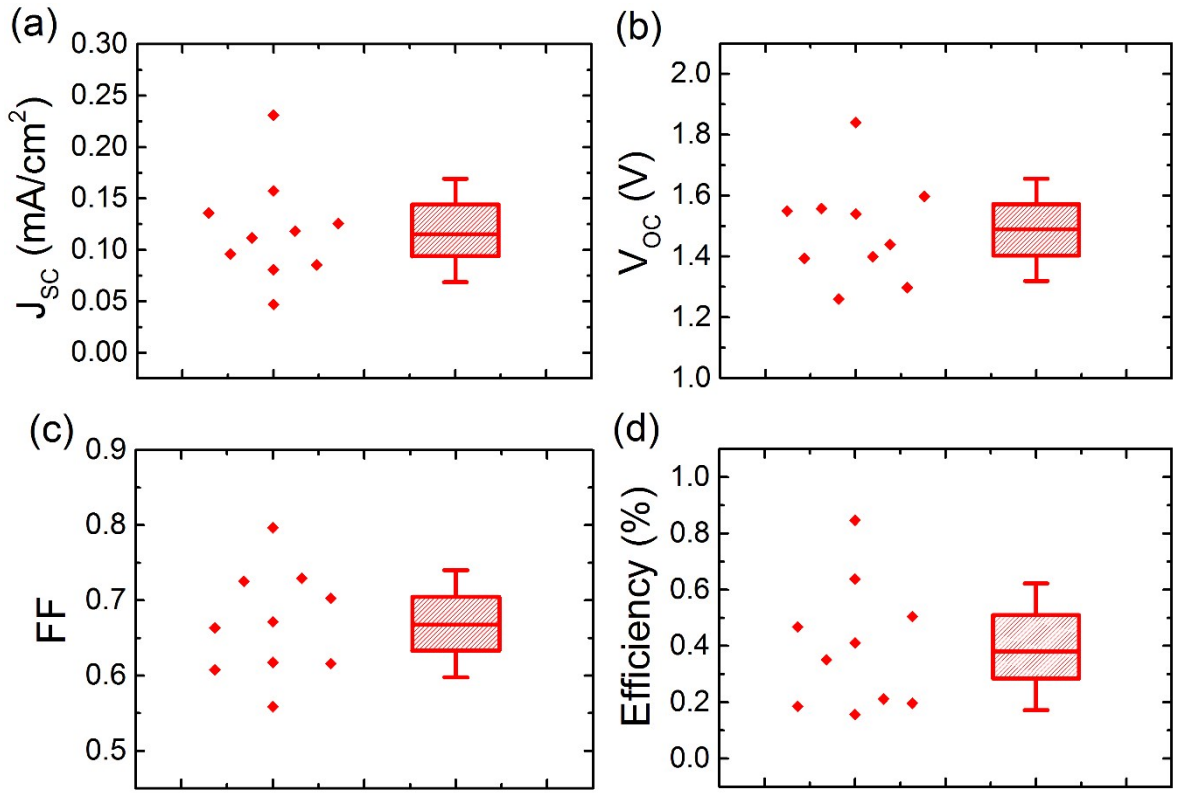

Fig. ESI14. Performance of several other cells, (a) J_{SC}, (b) V_{OC}, (c) FF, (d) efficiency. 6.1x4.2 in; double column, 600

Table ESI1. Summary of the different types of photovoltaic cells in which GQDs and CQDs are utilized and their performance characteristics

Material	Solar Cell	J_{SC} [mA/cm^2]	V_{OC} [V]	FF [%]	η [%]	Comment	Reference
GQD [a]	DSSC [b]	0.2	0.48	58	Not given	Low affinity of GQDs to TiO_2 and consequent poor charge injection	3
GQD	PSC [c]	3.51	0.61	53	1.14	Improved film morphology leads to enhancement of charge transport	4
GQD	PSC	0.92	0.77	27	0.19	Efficiency increased to 1.28 % after annealing. Non-optimized devices	5
CQD [d]	NRSC [e]	0.67	0.26	43	0.077	Different surface groups affect the device performance	6
N-CQD	DSSC	0.69	0.46	43	0.13	Nitrogen doping of the QDs increases the solar cell performance	7
CQD	NTSC [f]	0.02	0.58	35	0.004	Non-optimized electrolyte and electrodes	8
CQD	NRSC [g]	30.09	0.51	59	9.1	Device performance depended on CQD shell thickness with 5 layer giving the best results	9
CQD	PSC	8.4	0.61	62	3.18	CQD composite was spin cast on the underside of the solar cell improving light absorption	10

CQD	PSC	13.61	0.87	59.5	7.05	Improved charge separation and transport	11
CQD	PSC	0.29	1.59	48.5	0.23	Low efficiency ascribed to insulating nature of the CQD ligands	12
CQD	QDSC [h)]	1.88	0.605	31	0.35	CQDs improve charge transfer and transport	13
CQD	SMSC [i)] PSC	13.32 10.25	0.904 0.609	63.7 54.8	7.78 3.52	CQDs as the electron transport layer improve charge transport and collection efficiency	14
S-CQD [j)]	PSC	3.19	0.617	37	0.73	Presence of S atoms at the surface may improve efficiency	15
CQD	DSSC	0.53	0.38	64	0.13	Emissive trap sites act as recombination centers that contribute to low current	16

[a)] GQD: Graphene Quantum Dots, [b)] DSSC: Dye Sensitized Solar Cell, [c)] PSC: Polymer Solar Cell, [d)] CQD: Carbon Quantum Dots, [e)] NRSC: Nanorod Solar Cell, [f)] NTSC: Nanotube Solar Cell, [g)] NRSC: Nanorod Solar Cell, [h)] QDSC: Quantum Dot Solar Cell, [i)] SMSC: Small Molecule Solar Cell, [j)] S-CQD: Sulphur doped Carbon Quantum Dots

1 D. Qu, M. Zheng, L. Zhang, H. Zhao, Z. Xie, X. Jing, R. E. Haddad, H. Fan and Z. Sun, *Sci. Rep.*, 2014, **4**, 5294.

2 S. Zhu, Q. Meng, L. Wang, J. Zhang, Y. Song, H. Jin, K. Zhang, H. Sun, H. Wang and B. Yang, *Angew. Chemie Int. Ed.*, 2013, **52**, 3953–3957.

3 X. Yan, X. Cui, B. Li and L. S. Li, *Nano Lett.*, 2010, **10**, 1869–1873.

4 V. Gupta, N. Chaudhary, R. Srivastava, G. D. Sharma, R. Bhardwaj, S. Chand, N. S. R. S. G. D. B. R. Gupta Vinay Chaudhary and S. Chand, *J. Am. Chem. Soc.*, 2011, **133**, 9960–9963.

5 Y. Li, Y. Hu, Y. Zhao, G. Shi, L. Deng, Y. Hou and L. Qu, *Adv. Mater.*, 2011, **23**, 776–780.

6 J. Briscoe, A. Marinovic, M. Sevilla, S. Dunn and M. Titirici, *Angew. Chemie Int. Ed.*, 2015, **54**, 4463–4468.

7 Y.-Q. Zhang, D.-K. Ma, Y.-G. Zhang, W. Chen and S.-M. Huang, *Nano Energy*, 2013, **2**, 545–552.

8 M. Sun, X. Ma, X. Chen, Y. Sun, X. Cui and Y. Lin, *RSC Adv.*, 2014, **4**, 1120–1127.

9 C. Xie, B. Nie, L. Zeng, F.-X. Liang, M.-Z. Wang, L. Luo, M. Feng, Y. Yu, C.-Y. Wu, Y. Wu and S.-H. Yu, *ACS Nano*, 2014, **8**, 4015–4022.

10 J. J. Huang, Z. F. Zhong, M. Z. Rong, X. Zhou, X. D. Chen and M. Q. Zhang, *Carbon N. Y.*, 2014, **70**, 190–198.

11 C. Liu, K. Chang, W. Guo, H. Li, L. Shen, W. Chen and D. Yan, *Appl. Phys. Lett.*, 2014, **105**, 73306-1-73306–4.

12 W. Kwon, G. Lee, S. Do, T. Joo and S.-W. Rhee, *Small*, 2014, **10**, 506–513.

13 R. Narayanan, M. Deepa and A. K. Srivastava, *J. Mater. Chem. A*, 2013, **1**, 3907.

14 H. Zhang, Q. Zhang, M. Li, B. Kan, W. Ni, Y. Wang, X. Yang, C. Du, X. Wan and Y. Chen, *J. Mater. Chem. C*, 2015, **3**, 12403–12409.

15 S. Chandra, P. Patra, S. H. Pathan, S. Roy, S. Mitra, A. Layek, R. Bhar, P. Pramanik and A. Goswami, *J. Mater. Chem. B*, 2013, **1**, 2375–2382.

16 P. Mirtchev, E. J. Henderson, N. Soheilnia, C. M. Yip and G. A. Ozin, *J. Mater. Chem.*, 2012, **22**, 1265–1269.